PHYSICAL REVIEW B VOLUME 45, NUMBER 2 1 JANUARY 1992-II

Optical and magnetic-circular-dichroism–optically-detected-magnetic-resonance study of the Co^{2+} ion in $LiGa_5O_8$

J. F. Donegan
Department of Experimental Physics, University College, Galway, Ireland;
Optronics Ireland Research Centre and Department of Pure and Applied Physics, Trinity College, Dublin 2, Ireland;
and Sherman Fairchild Laboratory and Physics Department, Lehigh University, Bethlehem, Pennsylvania 18015

F. G. Anderson
Department of Experimental Physics, University College, Galway, Ireland
and Sherman Fairchild Laboratory and Physics Department, Lehigh University, Bethlehem, Pennsylvania 18015

F. J. Bergin, T. J. Glynn, and G. F. Imbusch
Department of Experimental Physics, University College, Galway, Ireland

(Received 19 June 1991)

Optical and magnetic-circular-dichroism–optically-detected-magnetic-resonance studies have been carried out on Co-doped $LiGa_5O_8$. The Co ions are found to be predominantly in the 2+ charge state and to substitute for tetrahedrally coordinated Ga^{3+} in the $LiGa_5O_8$ lattice, in sites which are shown to have C_3 point-group symmetry. The strong absorption bands from the ground state ${}^4A_2({}^4F)$ to the excited states ${}^4T_1({}^4P)$ and ${}^4T_1({}^4F)$ are each split by the low-symmetry C_3 field. A combination of the low-symmetry field and spin-orbit coupling is responsible for the ground-state splitting of $19.5\pm0.5\ \mathrm{cm}^{-1}$ observed by fluorescence line narrowing. Strong broadband luminescence is observed from the ${}^4T_1({}^4P)$ level to three lower levels, ${}^4A_2({}^4F)$, ${}^4T_2({}^4F)$, and ${}^4T_1({}^4F)$, with a lifetime that is constant at 200 ns from 10 K up to room temperature. The optically-detected magnetic-resonance studies show that the Co^{2+} ions are in sites which have axial symmetry along $\langle 111\rangle$-type axes of the unit cell, indicative of the C_3 symmetry present in these substitutional sites. We give a detailed crystal-field model for the Co^{2+} ion in the C_3 site in $LiGa_5O_8$ and deduce the crystal-field parameters from our experimental data.

I. INTRODUCTION AND BACKGROUND

When cobalt (Co) is added as a dopant to wide band-gap oxide materials, they acquire a characteristic color due to electronic transitions on the Co ions in the visible region of the spectrum. The cobalt ions are generally found in the 2+ and 3+ charge states in these oxide hosts. In 1961, Pappalardo, Wood, and Linares[1] carried out a study of the spectroscopic properties of cobalt in a number of oxide crystals. They investigated cobalt doping of MgO and ZnO, which offer full octahedral and tetrahedral symmetry for the dopant Co ions, respectively. These are therefore ideal test systems to establish the spectroscopic properties of dopant Co ions in oxide materials. The simplicity of the observed spectra allowed Pappalardo *et al.*[1] to perform a detailed crystal-field analysis of the spectra. These researchers also carried out investigations of cobalt-doped spinel ($MgAl_2O_4$) and YAG ($Y_3Al_5O_{12}$), each of which offer both tetrahedral and octahedral environments for the dopant Co ions. On the basis of the work in $MgO{:}Co^{2+}$ and $ZnO{:}Co^{2+}$, they found that their spinel and YAG samples were dominated by Co^{2+} spectra and that, given a choice, the Co^{2+} ions greatly preferred tetrahedral to octahedral coordination in these materials. A subsequent study of Co absorption spectra in garnet hosts was carried out by Wood and Remeika[2] in 1967. The observed spectra were ascribed to Co^{2+} and Co^{3+} ions, mainly in distorted tetrahedral environments. The tetrahedral Co^{3+} spectrum observed in the garnet material YAG is dominated by a broad double-peaked band centered near 9000 cm^{-1}. On the other hand, the tetrahedral Co^{2+} spectrum in YAG shows three absorption regions. The strongest absorption occurs in the visible peaking near 16 000 cm^{-1}, giving the YAG:Co samples a characteristic blue color, and two absorption bands occur in the near infrared, peaking at 7100 and 4700 cm^{-1}.

The material $LiGa_5O_8$ crystallizes with the spinel ($MgAl_2O_4$) structure, which is adopted by a large number of compounds whose general formula is XY_2O_4. In general, two types of spinel are distinguished: "normal" and "inverse," and the cube in Fig. 1 represents the unit cell of normal spinel. For convenience, the cell is divided into octants, and the arrangements of ions in two of the octants are shown. These arrangements are repeated in alternate octants. The octahedral and tetrahedral sites may be distinguished in this figure. Whereas in normal spinel the octahedral and tetrahedral sites are occupied by trivalent and divalent ions, respectively, in inverse spinel one-half of the trivalent ions occupy tetrahedral sites while the other half, together with the divalent ions, occupy octahedral sites, and the structure can be represented by the formula $Y(XY)O_4$.

The $LiGa_5O_8$ arrangement is a variation of the inverse

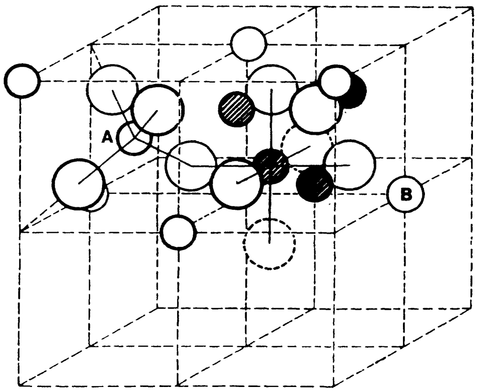

FIG. 1. Schematic diagram of the unit cell of normal spinel ($MgAl_2O_4$). For clarity, only two octants of the unit cell are shown. The large open circles are the oxygen ions, the small open circles are the tetrahedrally coordinated ions, and the hatched circles are the octahedrally coordinated ions. Atoms A and B in the figure are in tetrahedrally coordinated environments.

spinel structure and contains 4 formula units in the cubic cell shown in Fig. 1. The monovalent Li^+ ions and three-fifths of the Ga^{3+} ions are distributed among the octahedral sites in an ordered manner so that each row of octahedral ions in a $\langle 110 \rangle$-type direction contains a lithium ion in every fourth position.[3] This distribution of Li ions results in the arrangement shown in Fig. 2 for the second-nearest-neighbor shell of cations about a gallium ion in the tetrahedrally coordinated site. The nearest-neighbor oxygen ions are not shown. The Li ions are arranged symmetrically about the $[1\bar{1}1]$ direction of the cell. This arrangement of the Li ions means that the site symmetry for the tetrahedrally coordinated Ga^{3+} ions is reduced from T_d to C_3, and, as we will see later, the Co^{2+} ions substitute for Ga^{3+} at these sites in $LiGa_5O_8$. There are four possible inequivalent Co^{2+} sites in the unit cell, with C_3 axes along $\langle 111 \rangle$-type directions. The crystal structure of $LiGa_5O_8$ has been described in detail by Gorter.[4]

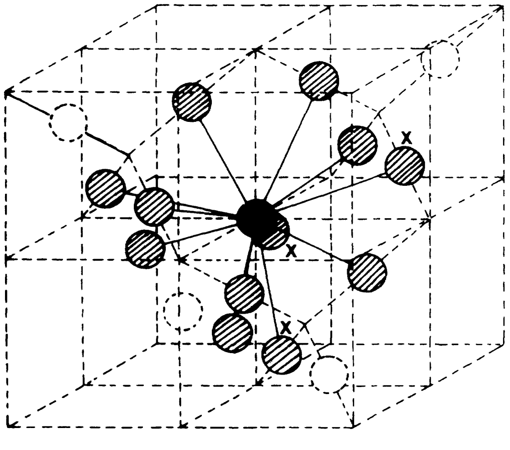

FIG. 2. Environment of the Co^{2+} ion in $LiGa_5O_8$ showing the shell of second-nearest-neighbor cations. This cube in this figure is shifted by a distance equal to half the cube edge with respect to the cube in Fig. 1 (so that the atom marked B in Fig. 1 is now at the center of the cell) and the oxygen nearest-neighbor ions are omitted for clarity. The solid circle is the Co^{2+} ion and the hatched circles are the octahedrally coordinated second-nearest-neighbor ions. The circles marked X are the Li^+ ions. The C_3 symmetry axis for the Co^{2+} ion in the center of the shell is the $[1\bar{1}1]$ direction.

In the past, extensive optical spectroscopic studies have been carried out on Cr^{3+}, Mn^{4+}, Fe^{3+}, and Ni^{2+} ions in $LiGa_5O_8$.[5–9] In this study we have combined optical and magnetic-circular-dichroism–optically-detected-magnetic-resonance (MCD-ODMR) spectroscopies to obtain a detailed account of the electronic structure and environment of the Co^{2+} ion in $LiGa_5O_8$. The experimental results are consistent with the C_3 site symmetry expected for substitutional Co^{2+} in the tetrahedrally coordinated sites in this material. A crystal-field model is developed for the Co^{2+} ion in $LiGa_5O_8$, and values for the crystal-field parameters are derived from the data.

II. EXPERIMENTAL DETAILS

The luminescence and excitation measurements were carried out in an Air-Products flow cryostat with temperatures in the range 10–300 K. An Aviv spectrophotometer was used for the absorption experiments along with a cold-finger cryostat with liquid-N_2 cooling. For the luminescence work, an Ar^+ laser with 100-mW power at 514.5 nm was employed. The excitation spectra were recorded using a cw dye laser with DCM or RG6 as the active dye medium. Both photomultipliers (with S20 and GaAs photocathodes) and a liquid-N_2-cooled Ge detector were used to monitor the light signals.

The MCD and ODMR experiments are illustrated in Fig. 3. In this illustrative example, the ground and excit-

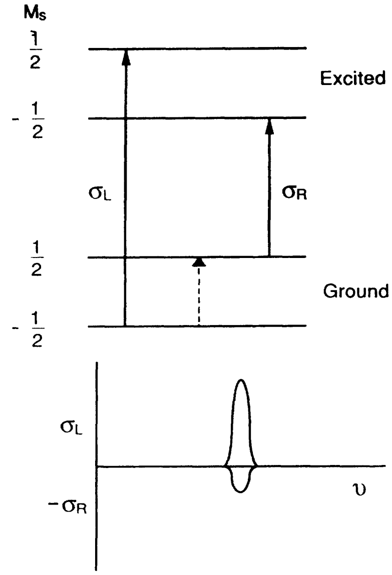

FIG. 3. An illustrative example of MCD with the ground and excited states both described by $S=\frac{1}{2}$. The lower Zeeman level in the ground state is more heavily populated than the upper state at low temperature, giving rise to a MCD signal. The ODMR transition in the ground state is indicated by a dashed line.

ed states are spin doublets, and these are each split into two by the magnetic field. The two circularly polarized absorption transition, σ_L and σ_R, are shown. These are transitions in which the light travels along the direction of the magnetic field. The oscillator strength of the two transitions are equal, but the absorption strength will depend on the populations in the ground-state sublevels. In this case, where there is a greater population in the lower level, in accordance with the Boltzmann formula, then σ_L will be greater than σ_R and the MCD signal, which is proportional to $(\sigma_L - \sigma_R)$, will be nonzero.

If now the sample is irradiated with microwave power at a frequency corresponding to the Zeeman splitting of the ground state, this will tend to equalize the populations in the two levels and there will be a *decrease* in the MCD signal. Thus, the ground-state resonance condition shows up as a change in the optical signal and this constitutes the optically-detected-magnetic-resonance signal.

The MCD-ODMR experiments were carried out at 1.6 K in an Oxford Instruments SM-3 superconducting magnet cryostat. The sample was mounted at the center of a 35-GHz TE_{011} microwave cavity having optical access. A Hinds SM-3 quartz modulator produced alternating left and right circularly polarized light at 50.3 kHz. The MCD signals were detected using both Si and Ge detectors combined with standard lock-in techniques. For the ODMR experiments, ~50 mW of microwave power was introduced into the cavity. For the case in which the absorption coefficients σ_L and σ_R are small, the MCD signal is given by

$$\text{MCD} = (\sigma_L - \sigma_R) \propto (I_R - I_L) , \qquad (1)$$

where I_L and I_R are the transmitted intensities for left and right circularly polarized light.

The samples of LiGa_5O_8 used in this study were grown by the flux method, and the dopant cobalt ions exhibit two zones of concentration in the material: a deep blue core and an outer pale blue region. Electron microprobe measurements of the cobalt concentration in one sample gave 0.5% in the core and 0.12% in the pale area.[10] All measurements were carried out on samples cut from the lightly doped region. For the magnetic resonance experiments a small sample (dimensions 1 mm×1 mm×1.5 mm) was cut so that it could be positioned in the microwave cavity with the magnetic field in the $(01\bar{1})$ plane.

III. EXPERIMENTAL RESULTS

The LiGa_5O_8:Co^{2+} system shows two regions of strong absorption, and their spectra recorded at 85 K are shown in Fig. 4. These spectra show a very strong similarity to those of Co^{2+} ions in tetrahedrally coordinated environments in $\text{Y}_3\text{Al}_5\text{O}_{12}$ and ZnAl_2O_4.[2,11] A Tanabe-Sugano energy level diagram for the lowest energy levels of a d^7 ion in a tetrahedral crystal field is also given in Fig. 4, and we assign the visible absorption band to the ${}^4A_2({}^4F) \rightarrow {}^4T_1({}^4P)$ transition and the infrared band to the ${}^4A_2({}^4F) \rightarrow {}^4T_1({}^4F)$ transition. A third absorption transition due to the ${}^4A_2({}^4F) \rightarrow {}^4T_2({}^4F)$ transition, expected to lie in the region of 4000 cm^{-1}, could not be detected even in samples with nominal Co concentration of 1%. The weak band in Fig. 4 with a zero-phonon line at 13 580 cm^{-1} is tentatively assigned to Co^{3+} in the octahedrally coordinated site in LiGa_5O_8 by comparison with previous studies of Co-doped $\text{Y}_3\text{Al}_5\text{O}_{12}$.[2]

On inspection of Fig. 4 we see that both absorption bands are split; the band in the visible has two broad components at 15 400 and 16 600 cm^{-1}, while the band in

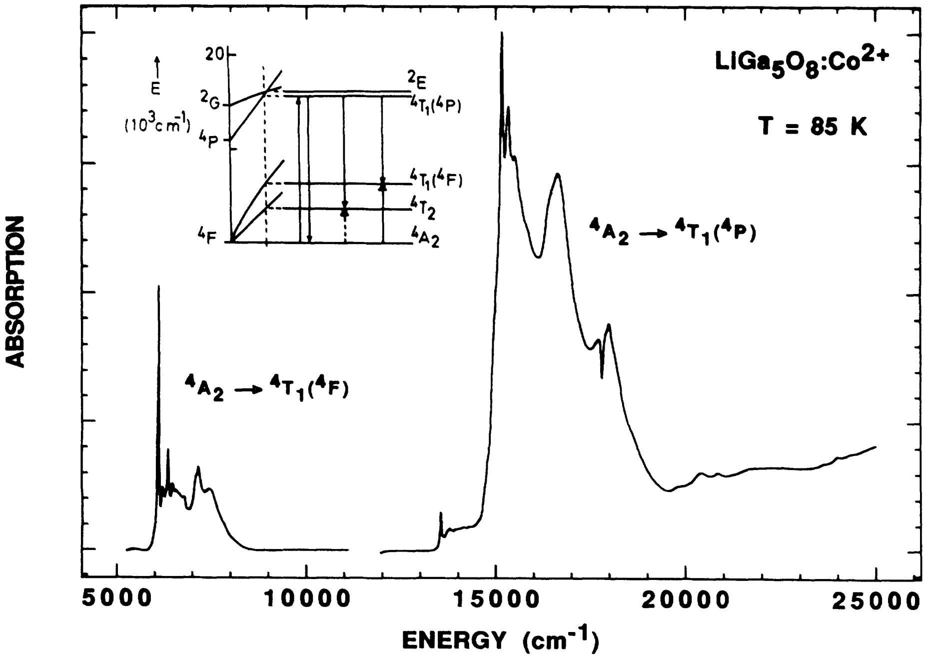

FIG. 4. The absorption spectrum of LiGa_5O_8:Co^{2+} recorded at 85 K showing the ${}^4A_2({}^4F) \rightarrow {}^4T_1({}^4P)$ and the ${}^4A_2({}^4F) \rightarrow {}^4T_1({}^4F)$ transitions. The inset shows a Tanabe-Sugano energy-level scheme for Co^{2+} in LiGa_5O_8. The absorption transitions are indicated on the energy-level scheme.

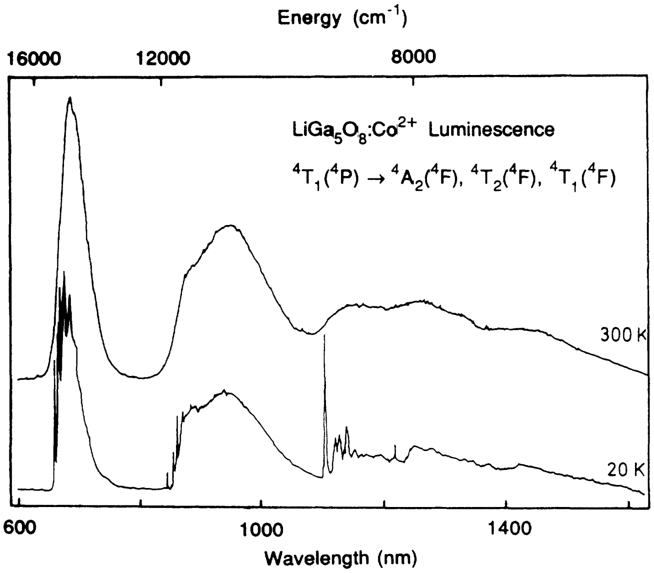

FIG. 5. The luminescence spectrum of $LiGa_5O_8:Co^{2+}$ recorded at 20 K and room temperature showing the three luminescence transitions. An Ar^+ laser with 100-mW power was used for excitation. The luminescence transitions are indicated on the energy-level scheme in Fig. 4.

the near infrared has two broad components at 7210 and 6300 cm^{-1}. A similar splitting was observed by Wood and Remeika in the corresponding Co^{2+} spectra in $Y_3Al_5O_{12}$.[2] There is some sharp-line structure evident in both transitions, which makes it difficult to unambiguously distinguish between electronic and vibrational fine structure.

Using Ar^+ laser excitation at 514.5 nm, three luminescence transitions are observed and the complete luminescence spectrum at 20 K and room temperature are shown in Fig. 5. This spectrum was recorded using a Ge detector and is not corrected for the system response. We note that, as the Ge detector has a poor response in the visible, the first luminescence transition in the red is much stronger than the other two. The zero-phonon line of the first luminescence transition at 15 157 cm^{-1} recorded at 15 K coincides with the first sharp peak of the visible absorption band in Fig. 4. All three luminescence bands of Fig. 5 are found to have the same excitation spectrum [recorded at 15 K and shown in Fig. 6(a)] and the same lifetime. Therefore, these are assigned to transitions originating on the same $^4T_1(^4P)$ level. The red luminescence is the $^4T_1(^4P)\rightarrow{}^4A_2(^4F)$ transition (see the energy-level diagram in Fig. 4) while the two near-infrared luminescence transitions in Fig. 5 are assigned to the

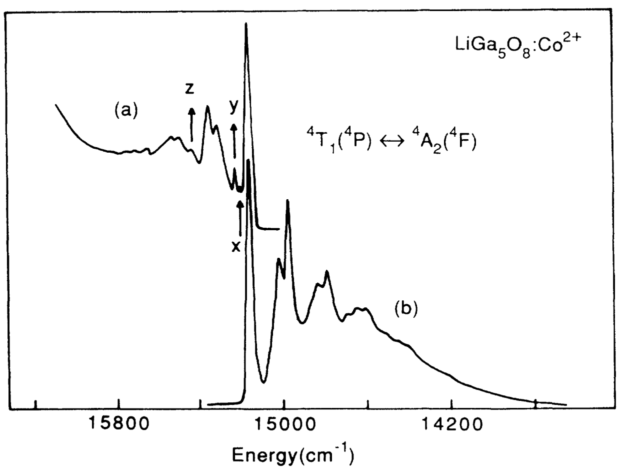

FIG. 6. (a) The excitation spectrum of all three luminescence transitions shown in Fig. 5 recorded at 15 K and (b) the $^4T_1(^4P)\rightarrow{}^4A_2(^4F)$ luminescence transition recorded at 15 K. These two spectra are clearly mirror images of one another apart from the features marked x, y, and z in the figure.

TABLE I. Comparison of the sideband features (in cm^{-1}) in luminescence and excitation of the $^4A_2(^4F)\leftrightarrow{}^4T_1(^4P)$ transitions for Co^{2+} ions in $LiGa_5O_8$.

Luminescence	Excitation
	46
	63
149	146
185	188
	277
333	340
374	378
474	460
520	507
564	565
630	626
657	
714	704
768	

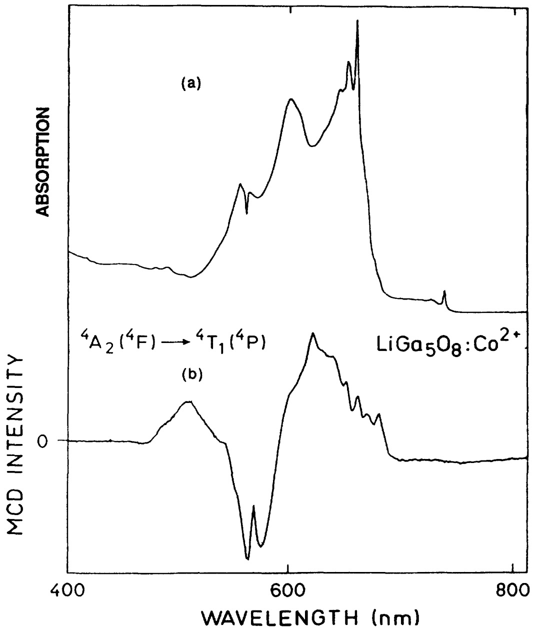

FIG. 7. (a) The $^4A_2(^4F)\rightarrow{}^4T_1(^4P)$ absorption transition recorded at 85 K. (b) The wavelength dependence of the MCD signal for the $^4A_2(^4F)\rightarrow{}^4T_1(^4P)$ transition recorded at 1.6 K. The sharp dip in the MCD signal at 566 nm is ascribed to a Fano antiresonance effect.

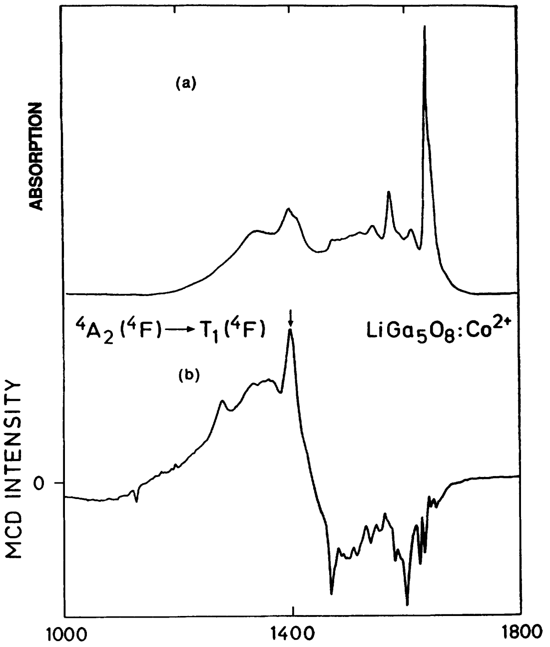

FIG. 8. (a) The ${}^4A_2({}^4F)\rightarrow{}^4T_1({}^4F)$ absorption transition recorded at 85 K. (b) The wavelength dependence of the MCD signal for the ${}^4A_2({}^4F)\rightarrow{}^4T_1({}^4F)$ transition recorded at 1.6 K.

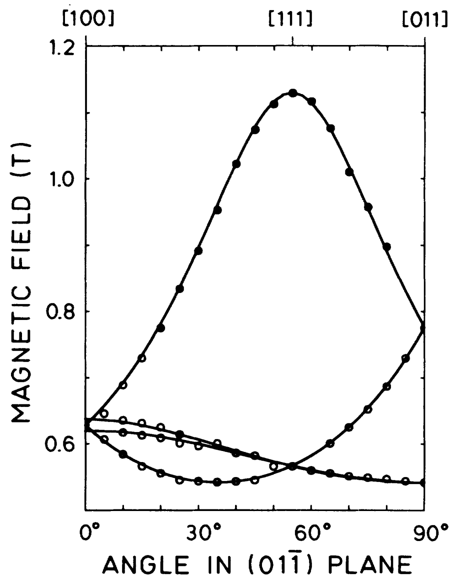

FIG. 10. The angular dependence of the ODMR signal with $\mathbf{B}\perp(01\bar{1})$. The C_3 symmetry for the Co^{2+} impurity is evident from the spectrum. The solid points are due to increases in the MCD signals at resonance and the open circles are due to decreases in the MCD signals at resonance. The splitting of the ODMR lines near [100] is due to a small misalignment (~2°) of the $LiGa_5O_8$:Co^{2+} crystal.

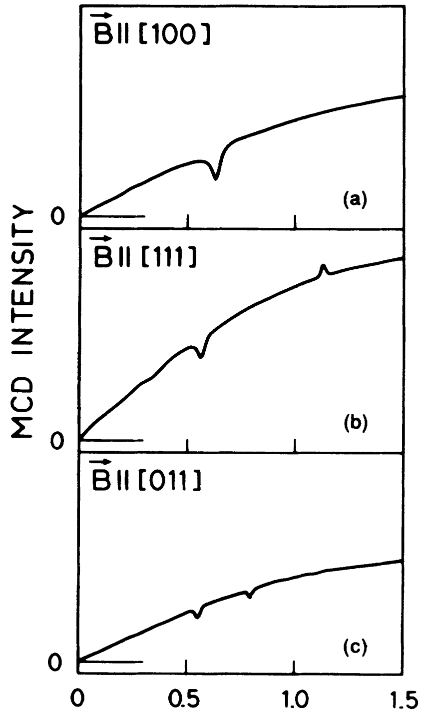

FIG. 9. The magnetic-field dependence of the MCD signal along the (a) [100], (b) [111], and (c) [011] directions recorded at the arrowed wavelength position (1400 nm) in Fig. 8. For comparison, the scaling of the y axis for the three signals is the same. The dips and peaks in the spectra are due to ODMR transitions. Note the "positive" ODMR transition for the [111]-oriented spectrum.

${}^4T_1({}^4P)\rightarrow{}^4T_2({}^4F)$ and ${}^4T_1({}^4P)\rightarrow{}^4T_1({}^4F)$ transitions, respectively. The lifetime of all the luminescence bands at 10 K was found to be 200±20 ns. This lifetime is constant up to room temperature within experimental error.

The red luminescence transition, recorded in greater detail at 15 K, is shown in Fig. 6(b) along with the luminescence excitation spectrum in Fig. 6(a). The two spectra in Fig. 6 are clearly mirror images of one another except for the features marked x, y, and z in the excitation spectrum. The frequencies (with respect to the zero-phonon line at 15 157 cm^{-1}) of all the fine-structure features in the spectra of Fig. 6 are given in Table I. The extra fine-structure lines in the excitation spectrum are at 46, 63, and 277 cm^{-1} from the zero-phonon line position.

In Figs. 7 and 8 we present the MCD spectra recorded at $B=1.64$ T and $T=1.6$ K for the $LiGa_5O_8$:Co^{2+} system along with the corresponding absorption transitions at $T=85$ K. The MCD spectra have not been corrected for the system response. The MCD band in Fig. 8(b) contains a great wealth of fine structure at this temperature, even more than is evident at 85 K in the absorption spectrum in Fig. 8(a). In the MCD spectrum of Fig. 7(b) there is a rather interesting feature at 566 nm. It is seen to be a "dip" in the MCD signal at this point. This feature is also observed as a dip in absorption strength in the absorption spectrum of Fig. 7(a).

The magnetic field variation of the MCD signal taken at $\lambda=1400$ nm along the [100], [111], and [011] directions is shown in Fig. 9. We note that the intensity of the MCD signal is not isotropic, as it would be if the Co^{2+} ion was at a site of full T_d symmetry. We find instead that it shows a maximum along the [111] direction [Fig.

9(b)], suggesting an axis of symmetry along this direction. In this figure we also show the ODMR transitions, identified as peaks and dips in the MCD signals. It is interesting to note that the high-field ODMR transition along [111] shows an *increase* in the strength of the MCD band.

The angular variation of the Co^{2+} ODMR transitions with the magnetic field **B** in the (011) plane is shown in Fig. 10. The solid points are due to ODMR transitions which show an increase in the total MCD signal (positive ODMR), and the open points are due to transitions which show a decrease in the MCD signal (negative ODMR). The "positive" ODMR signal is strongest along [111] and weakens quickly as the crystal is rotated towards either the [100] or [011] direction. The splitting of the ODMR lines near [100] is due to a small misalignment (~2°) of the $LiGa_5O_8{:}Co^{2+}$ crystal; the small size of the sample making alignment difficult.

IV. CRYSTAL-FIELD MODEL

In this section we describe our crystal-field model for the Co^{2+} center in $LiGa_5O_8$. This model includes a full treatment of the C_3 crystal field which acts upon the Co^{2+} ion. We start with the electron-electron interaction, and then include the crystal-field interaction. Lastly, we consider the spin-orbit interaction, which gives rise to a splitting of the ground state. This leads to an expression for the fine-structure parameter D for the ground state.

A. Electron-electron interaction

The Co^{2+} impurity in $LiGa_5O_8$ has the d^7 configuration, which we treat as a three-hole configuration. In accordance with Hund's rule, the ground-state term is a ^4F term. There is a second spin quadruplet, a ^4P term. In the case of a free Co^{2+} ion, the ^4P term is the first excited term, lying approximately 15 500 cm^{-1} above the ground term.[12] The ^4P-^4F splitting is reduced for the case of the Co^{2+} impurity in crystals, as a result of the greater extent of the wave functions when the ion is in a crystalline environment. We denote the ^4P-^4F splitting, which can be expressed in terms of the Racah parameter B, by the single parameter Δ.

B. Crystal-field interaction

1. T_d component

We decompose the crystal-field potential into two components, which we treat separately. The first component is a field of T_d symmetry, resulting primarily from the first shell of neighbors that consists of four oxygen ions in tetrahedral coordination about the Co^{2+} ion as shown in Fig. 1. In addition, the third shell of neighbors consists of four gallium ions also in tetrahedral coordination about the Co^{2+} ion. These gallium ions are located in the corners of the left-hand octant in Fig. 1. The tetrahedral crystal field splits the one-hole d states so that the t_2-symmetry holes are lower in energy than the e-symmetry holes by an amount $10Dq$. The partial removal of the fivefold degeneracy of the d states splits the ^4F term into three manifolds: $^4A_2$, $^4T_2$, and $^4T_1(^4F)$. The ^4P term spans the manifold $^4T_1(^4P)$. These splittings are shown in Fig. 11, which indicates schematically the effect of various perturbations on the Co^{2+} ion in $LiGa_5O_8$. The many-hole ($M_s=\frac{3}{2}$) states for these manifolds are given by

$$\begin{aligned}
&^4A_2=(\xi,\eta,\zeta)\ ,\\
&^4T_2=(\varepsilon,\eta,\xi)\ ,\\
&^4T_{1z}(^4F)=1/\sqrt{5}[(\xi,\eta,\theta)+2(\zeta,\theta,\varepsilon)]\ ,\\
&^4T_{1z}(^4P)=1/\sqrt{5}[2(\xi,\eta,\theta)-(\zeta,\theta,\varepsilon)]\ ,
\end{aligned}\tag{2}$$

where (X_1,X_2,X_3) denotes the Slater determinant of the orbitals X_1, X_2, and X_3. In addition, the tetrahedral crystal field gives rise to a mixing between the $^4T_1(^4F)$ and $^4T_1(^4P)$ manifolds, resulting in the repulsion of these levels, as shown in the middle of Fig. 11.

2. C_3 component

The second component of the crystal-field potential is a component of C_3 symmetry. The second shell of neighbors around the Co^{2+} impurity consists of nine gallium ions and three lithium ions arranged as shown in Fig. 2. If all the ions in the second shell were identical, i.e., gallium ions in this case, then the site symmetry would be T_d. It is the three lithium ions that are responsible for lowering the symmetry to C_3. Contrary to a note by Macfarlane,[13] there is a distinction between C_3 and C_{3v} potentials, though, like the C_{3v} potentials, the C_3 potential splits each orbital triplet into an orbital singlet and an orbital doublet. [We consider an expansion of the potential in terms of spherical harmonics. The linear combination of $L=4$ spherical harmonics (neglecting the $M=0$ har-

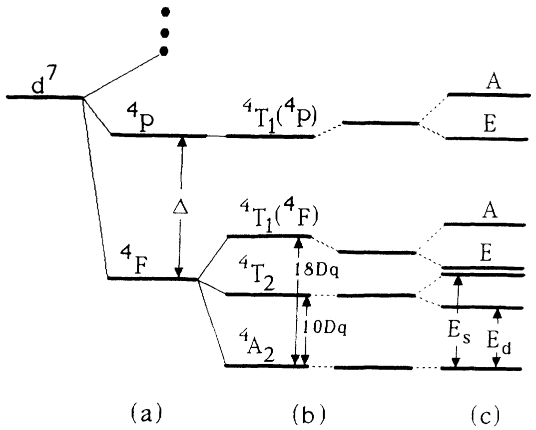

FIG. 11. Energy-level diagram showing the splittings of the d^7 configuration for the Co^{2+} impurity in $LiGa_5O_8$, due to (a) the electron-electron interaction, (b) the tetrahedral component of the crystal field, and (c) the C_3 component of the crystal field. The C_3 crystal field splits each orbital triplet (T_1,T_2) into a doublet (E) and a singlet (A). The energies E_D and E_S used in the determination of the fine-structure parameter D are also shown.

monic) which describes a C_{3v} potential is $(Y_{43}-Y_{4-3})$, which is proportional to $\cos(3\phi)$,[13] where ϕ is measured about the three-fold axis with $\phi=0$ defining one of the three reflection planes. Reflections through these planes change ϕ, but not $\cos(3\phi)$. In lowering the symmetry to C_3, an additional term must be added to the potential and this term does not remain unchanged with reflections through these three planes but retains the three-fold rational symmetry. The linear combination $(Y_{43}+Y_{4-3})$, which is proportional to $\sin(3\phi)$, is such a term. This additional term is the distinction between the C_{3v} and the C_3 potentials.[14]]

We write the one-electron C_3 potential within d states in terms of operators which span irreducible representations of the T_d point group. We find

$$V_{C_3}=\alpha A_1+V(T_{2\xi}+T_{2\eta}+T_{2\zeta})+W(T_{1x}+T_{1y}+T_{1z}) , \tag{3}$$

where α, V, and W are constants. Analytic expressions for these constants can be derived, for example, by assuming a point-ion model. However, we proceed by treating these as parameters. We note that it is the last term in Eq. (3) which distinguishes this potential from one of C_{3v} symmetry. We define the following reduced matrix elements for $i,j=\xi,\eta,\zeta$ and $k=\theta,\varepsilon$:

$$\begin{aligned}
&\langle t_{2i}|V_{C_3}|t_{2i}\rangle=\alpha_t ,\\
&\langle e_k|V_{C_3}|e_k\rangle=\alpha_e ,\\
&\langle t_{2i}|V_{C_3}|t_{2j}\rangle=v/3 \quad (i\neq j) ,\\
&\langle t_{2\zeta}|V_{C_3}|e_\theta\rangle=\sqrt{2/3}v' ,\\
&\langle t_{2\zeta}|V_{C_3}|e_\varepsilon\rangle=\sqrt{2/3}w .
\end{aligned} \tag{4}$$

The parameters α_t and α_e give a contribution, in addition to that of the tetrahedral component of the crystal field, to the splitting between the t_2 and e holes. We therefore incorporate this additional contribution into the parameter $10Dq$. The parameters v and v', which result from the $T_{2\xi}+T_{2\eta}+T_{2\zeta}$ operator, are defined following Macfarlane.[13] The parameter w results from the $T_{1x}+T_{1y}+T_{1z}$ operator, and so does not appear as a parameter for a C_{3v} potential. Using these parameters and Eq. (3) in conjunction with the Wigner-Eckart theorem, we have exactly prescribed the one-hole matrix elements of a C_3 potential within a basis of d holes. The nature of this potential is better understood if we make a change of basis for the t_2 states that reflects the axial nature ($\langle 111\rangle$-type directions) of the C_3 potential. Consider the basis set defined by

$$\begin{aligned}
&t_{2z}=1/\sqrt{3}(t_{2\xi}+t_{2\eta}+t_{2\zeta}) ,\\
&t_{2\theta}=1/\sqrt{6}(2t_{2\zeta}-t_{2\xi}-t_{2\eta}) ,\\
&t_{2\varepsilon}=1/\sqrt{2}(t_{2\xi}-t_{2\eta}) .
\end{aligned} \tag{5}$$

In the basis set of d states (t_{2z}, $t_{2\theta}$, $t_{2\varepsilon}$, e_θ, e_ε), the one-hole matrix elements of the C_3 potential are

$$\mathcal{H}_{C_3}=\begin{bmatrix} 2v/3 & 0 & 0 & 0 & 0\\ 0 & -v/3 & 0 & v' & w\\ 0 & 0 & -v/3 & -w & v'\\ 0 & v' & -w & 0 & 0\\ 0 & w & v' & 0 & 0 \end{bmatrix} . \tag{6}$$

From Eq. (6), we readily see the difference in how the C_{3v} and C_3 potentials act within d states. The parameter v' mixes the $t_{2\theta,2\varepsilon}$ states with $e_{\theta,\varepsilon}$ states in one sense, while the parameter w mixes these states in the opposite sense.

The matrix elements of the C_3 potential taken between the many-hole states of the four manifolds prescribed in Eq. (2) are readily determined from the one-hole matrix elements given in the previous paragraph. This results in a 10×10 matrix. This matrix can be reduced in to a 4×4 block and a 6×6 block through a change of basis for the orbital-triplet manifolds like that given in Eq. (5). Within the basis set $\{{}^4A_2, {}^4T_{1z}({}^4F), {}^4T_{2z}, {}^4T_{1z}({}^4P)\}$, the many-hole matrix elements of the *full* crystal-field interaction *and* the electron-electron interaction are

$$\mathcal{H}=\begin{bmatrix} -6G & I & -2J & 2I\\ I & 3G+2L & -4K & -2G+2N\\ -2J & -4K & -G+2H & 2K\\ 2I & -2G+2N & 2K & F+2M \end{bmatrix} . \tag{7}$$

Within the basis set $\{{}^4T_{1\theta}({}^4F), {}^4T_{1\varepsilon}({}^4F), {}^4T_{2\theta}, {}^4T_{1\theta}({}^4P), {}^4T_{1\varepsilon}({}^4P)\}$, the many-hole matrix elements of the crystal-field and electron-electron interaction are

$$\mathcal{H}=\begin{bmatrix} 3G-L & 0 & 2K & -P & -2G-N & -J\\ 0 & 3G-L & P & 2K & J & -2G-N\\ 2K & P & -G-H & 0 & -K & -Q\\ -P & 2K & 0 & -G-H & Q & -K\\ -2G-N & J & -K & Q & F-M & 0\\ -J & -2G-N & -Q & -K & 0 & F-M \end{bmatrix} . \tag{8}$$

The variables $F,G,H,\ldots,Q$ given above are defined by

$$\begin{aligned} &F=\Delta, \quad L=1/5(3v/2+2\sqrt{2}v')\ , \\ &G=2Dq, \quad M=1/5(v-2\sqrt{2}v')\ , \\ &H=v/6, \quad N=1/5(-v/3+3\sqrt{2}v'/2)\ , \\ &I=\sqrt{2/5}v', \quad P=1/\sqrt{5}(\sqrt{3}v/2+\sqrt{2}v')\ , \\ &J=w/\sqrt{2}, \quad Q=1/\sqrt{5}(-v+v'/\sqrt{2})\ , \\ &K=w/\sqrt{10}\ . \end{aligned} \tag{9}$$

From Eqs. (7) and (8), we can show that, as required by symmetry, the C_3 potential splits the orbital triplets into an orbital singlet and an orbital doublet, as shown in Fig. 11, and we can also show how the differences between the C_3 and C_{3v} potentials affect the mixing of the orbital triplets. Diagonalizing the matrices in Eqs. (7) and (8) yields the many-hole energy levels and eigenstates for the Co^{2+} impurity in the site of C_3 symmetry.

C. Spin-orbit interaction

The spin-orbit interaction has the effect of splitting in first order each of the orbital doublets into four Kramers doublets. (Note that $S=\frac{3}{2}$.) In addition, the spin-orbit interaction in second order splits the orbital singlets into two Kramers doublets. We concentrate on the splitting of the ${}^4A_2$ ground manifold.

The spin-orbit interaction mixes the ${}^4A_2$ ground manifold with the ${}^4T_2$ manifold. The many-hole matrix elements of the orbital angular momentum L taken between the states of these two manifolds is characterized by

$$\langle T_{2\zeta}|L_z|A_2\rangle=2i, \quad i=\sqrt{-1}\ . \tag{10}$$

This matrix element is unchanged if we transform to the basis set for the ${}^4T_2$ manifold defined by Eq. (5) and perform a similar transformation on the orbital momentum operators. For example, we define L_z', by

$$L_z'=1/\sqrt{3}(L_x+L_y+L_z)\ , \tag{11}$$

which yields

$$\langle T_{2z}|L_z'|A_2\rangle=2i \tag{12}$$

and similarly for $T_{2\theta}$ and $T_{2\epsilon}$ with L_x' and L_y', respectively.

We neglect for the moment the mixing of the ${}^4T_2$ manifold with the other orbital-triplet manifolds, but consider only the splitting, due to the C_3 symmetry field, of this manifold into an orbital doublet, at an energy E_D above the ${}^4A_2$ manifold, and an orbital singlet, at an energy E_S above the ${}^4A_2$ manifold. The spin-orbit interaction between the ${}^4T_2$ and ${}^4A_2$ manifolds splits the ${}^4A_2$ manifold into two Kramers doublets. One doublet is comprised of the $M_s=\pm\frac{3}{2}$ states, the second of the $M_s=\pm\frac{1}{2}$ states. The second-order energies of these two doublets are given by

$$\begin{aligned} &E(\pm\tfrac{3}{2})=-3\lambda^2(3/E_S+2/E_D)\ , \\ &E(\pm\tfrac{1}{2})=-\lambda^2(1/E_S+14/E_D)\ , \end{aligned} \tag{13}$$

where λ is the many-electron spin-orbit parameter. For the free Co^{2+} ion, λ is approximately $-180\ \text{cm}^{-1}$.[15] For the ion in a crystalline environment, λ is somewhat reduced (typically to 0.8 of the free-ion value) from this value.

The ground-state fine-structure parameter denoted D is a measure of the splitting between the two Kramers doublets within the ground ${}^4A_2$ manifold. We now include the mixing of the ${}^4T_2$ manifold with the other orbital-triplet manifolds. We define the fraction of the ${}^4T_2$ wave function within the ith $(i=1,2,3)$ orbital doublet to be β_i, and the fraction of the ${}^4T_2$ wave function in the ith orbital singlet (neglecting the ${}^4A_2$) to be α_i. We find then that D is given by

$$\begin{aligned} D&=\tfrac{1}{2}[E(\pm\tfrac{3}{2})-E(\pm\tfrac{1}{2})] \\ &=4\lambda^2\left[\sum_{i=1}^{3}\beta_i\Big/E_{D_i}-\sum_{i=1}^{3}\alpha_i\Big/E_{S_i}\right]\ . \end{aligned} \tag{14}$$

Since the fine-structure splitting is large compared with the Zeeman splitting as measured here by ODMR, we can treat the two Kramers doublets resulting from the ${}^4A_2$ manifold independently, with each doublet being described by an effective spin $S'=\frac{1}{2}$. The effective-spin Hamiltonian for each of the doublets is

$$\mathcal{H}_{\text{eff}}=\mu_B\mathbf{B}\cdot\mathbf{g}\cdot\mathbf{S}'\ . \tag{15}$$

The g tensor has two independent components: $g_\parallel$ (along the three-fold axis) and $g_\perp$ (perpendicular to the three-fold axis). In first order, the g values in the $\pm\frac{3}{2}$ manifold are $g_\parallel=3g_e$ $(g_e=2.0023)$ and $g_\perp=0$. The g values in first order in the $\pm\frac{1}{2}$ manifold are $g_\parallel=g_e$ and $g_\perp=2g_e$.[16]

Departures of the experimental g values from these theoretical values within the $M_s=\pm\frac{1}{2}$ manifold are explained using the usual second-order corrections involving the spin-orbit interaction and the orbital Zeeman interaction. As with the fine-structure splitting, the mixing with excited states involves the states of the ${}^4T_2$ manifold. We find that

$$\begin{aligned} &g_\parallel=g_e-8\lambda\sum_{i=1}^{3}\alpha_i\Big/E_{S_i}\ , \\ &g_\perp=2\left[g_e-8\lambda\sum_{i=1}^{3}\beta_i\Big/E_{D_i}\right]\ . \end{aligned} \tag{16}$$

The results in Eq. (16) have a similar form to those in Eq. (14). Indeed, we can relate the g values to the fine-structure parameter by

$$g_\perp/2-g_\parallel=-2D/\lambda\ . \tag{17}$$

V. ANALYSIS OF RESULTS AND DISCUSSION

We now proceed with the analysis of our experimental data in light of the theory developed in the previous section and of the assignments made for the observed optical transitions in Sec. III. We noted that both absorption transitions in Fig. 4 show a splitting into two bands; this splitting is due to the C_3 crystal field present at the Co^{2+}

site. The additional band with a peak at 18 200 cm^{-1} in Fig. 4 is most likely due to higher-lying levels arising from the ^2G free-ion level as shown in the energy-lying diagram in Fig. 4.[17] Values for Δ and $10Dq$ can be estimated by fitting the average energies of the $^4A_2(^4F)\rightarrow{}^4T_1(^4P)$ and $^4A_2(^4F)\rightarrow{}^4T_1(^4F)$ transition. The experimental positions we choose for the fitting process are at 6300, 7210 cm^{-1} for the $^4A_2(^4F)\rightarrow{}^4T_1(^4F)$ transition and 15 400, 16 600 cm^{-1} for the $^4A_2(^4F)\rightarrow{}^4T_1(^4P)$ transition. Choosing these positions is somewhat difficult due to the presence of much vibrational structure in these spectra. Values for v, v', and w are then chosen and the matrices in Eqs. (7) and (8) are diagonalized iteratively until a good fit to the experimental positions is found. The following values are found from our analysis:

$$\begin{gathered}\Delta=+10\,781\ \mathrm{cm}^{-1},\quad v=+1362\ \mathrm{cm}^{-1}\,,\\ 10Dq=+3770\ \mathrm{cm}^{-1},\quad v'=-10\ \mathrm{cm}^{-1}\,,\\ w=\pm 20\ \mathrm{cm}^{-1}\,.\end{gathered}\tag{18}$$

These values give an excellent fit to the experimental positions. Hund's rule requires that the ground state be the ^4F term; so we require Δ to be positive. The strong tetrahedral component of the crystal field, coming primarily from the four nearest-neighbor oxygen ions, determines the sign of $10Dq$. These oxygen ions are negatively charged. The lobes of the t_2-symmetry *hole* orbitals are closer to the oxygen ions than the lobes of the e-symmetry *hole* orbitals. Hence, the t_2-symmetry holes are lower in energy than the e-symmetry holes, making $10Dq$ positive. Setting the signs of these parameters we find that the signs of v and v' are determined to be positive and negative, respectively. The fit to the data is insensitive to the sign of w. This fitting procedure suggests that, for each orbital triplet, the doublet is shifted down in energy and the singlet shifted up in energy by the C_3 crystal field.

The positive sign of v is physically reasonable. In an ionic model, the gallium ions possess a $+3e$ charge and the lithium ions a $+1e$ charge. Hence, the perturbation potential resulting from the lithium ions is that of three *negatively* charged ions in a C_3 symmetry configuration. The lobes of the t_{2z} hole orbital lie in a plane perpendicular to the C_3 symmetry axis and the lobes of the $t_{2\theta}$ and $t_{2\varepsilon}$ hole orbitals, are therefore closer to the lithium ions. Hence, these latter two orbitals have a lower energy than the t_{2z} orbital. Equation (6) therefore implies that v is positive.

The signs of v' and w are much harder to explain in physical terms. We note, however, that, in the point-ion model for this defect, v' is predicted to have a sign opposite to that of v, and w is predicted to have the same sign as v. We recall that the sign of w is not determined in our fit. In any event, both v' and w are found to be small in our case.

An interesting feature of this Co^{2+} system is the sharp dip observed at 566 nm in the absorption spectrum in Fig. 7(a) and in the MCD signal of Fig. 7(b). We believe that the dip is due to Fano antiresonance effect such as has been observed in $\mathrm{KMgF_3}{:}V^{2+}$ and in Cr^{3+} doped glasses.[18,19] Consulting the Tanabe-Sugano diagram for a d^7 ion in tetrahedral symmetry,[17] we find that there are a number of levels originating on the free-ion ^2G level which are expected to lie in this general spectral region. We are unable to make any definitive electronic assignment for the antiresonance feature.

The width of the zero-phonon 15 157-cm^{-1} line of the $^4T_1(^4P)$ level in luminescence is 24 cm^{-1} (full width at half maximum) at 15 K. A series of nonresonant fluorescence line narrowing (FLN) experiments were performed in order to investigate structure hidden within this large inhomogeneous profile. The detailed results of this investigation have been published elsewhere.[20] From these FLN measurements, the ground-state splitting due to a combination of the C_3 crystal field and spin-orbit coupling is 19.5 cm^{-1}, from which we obtain $D=9.75\ \mathrm{cm}^{-1}$.

The optical spectra in Figs. 4–8 show a considerable number of sharp-line features. As indicated above, each of the crystal-field levels is further split by spin-orbit coupling, the doublet into four components and the singlet into two components. As a result the $^4A_2(^4F)\rightarrow{}^4T_1(^4P)$ absorption spectrum in Fig. 4 should contain *six* electronic components among a large number of vibrational sideband features. It is difficult to identify transitions to these electronic levels in the absorption spectra shown in Fig. 4 which were taken at 85 K. However, in the excitation spectrum of the $^4T_1(^4P)\rightarrow{}^4A_2(^4F)$ luminescence transition shown in Fig. 6(a), recorded at 15 K under much higher resolution, the features labeled x,y,z are clearly electronic as they are not observed in the corresponding luminescence spectrum. We tentatively identify the line at 15 157 cm^{-1} and the features at 46, 63, and 277 cm^{-1} above 15 157 cm^{-1} as the spin-orbit split components of the orbital doublet level coming from $^4T_1(^4P)$. The possible presence of levels arising from the ^2G free-ion level in this spectral region is a complicating factor making our identification rather tentative. The $^4A_2(^4F)\rightarrow{}^4T_1(^4F)$ transition in Figs. 4 and 8 is particularly rich is spectral features making identification of the six expected electronic components very difficult. Nevertheless, we can reasonably assign the lines at 6060 and 7140 cm^{-1} to electronic transitions.

The very fast radiative decay time of the luminescence transitions at low temperature indicates that these transitions have a strong electric dipole character and, consequently, have a large oscillator strength. This comes about because, in the tetrahedral site (in which the site symmetry is C_3), in $\mathrm{LiGa_5O_8}$ the odd-parity crystal field mixes the $3d$ states of Co^{2+} with higher-energy states of opposite parity, and this mixing is responsible for the electric-dipole character of this transition. The lack of discernible change in the lifetime up to room temperature indicates the absence of a competing nonradiative decay process for this level and strongly suggests that the luminescence process is very efficient. The room-temperature luminescence spectrum in Fig. 5 shows three broadbands which have high luminescence efficiency. In contrast to both $\mathrm{ZnO{:}Co}^{2+}$ (Ref. 21) and $\mathrm{ZnAl_2O_4{:}Co}^{2+}$ (Ref. 11), the luminescence bands in Fig. 5 originate on the $^4T_1(^4P)$ level rather than the ^2E level. From the

Tanabe-Sugano diagram[17] we find that luminescence transitions originating on the $^4T_1(^4P)$ are very broad due to the sensitivity of the $^4T_1(^4P)$ level to the crystal-field environment. Luminescence transitions from the ^2E level consist of sharp lines due to its insensitivity to the crystal field. The three luminescence transitions observed in $LiGa_5O_8$:Co^{2+} are also spin allowed, which contributes to their large oscillator strength. The combination of broad luminescence transitions coupled with a large oscillator strength makes $LiGa_5O_8$:Co^{2+} an ideal candidate for a tunable solid-state laser in the visible and near infrared.

The "positive" ODMR lines in Figs. 9 and 10 are an interesting feature of these samples. We would intuitively feel that the ODMR transition should equalize the populations of the ground-state levels as illustrated in Fig. 3 and thereby cause a reduction of the MCD signals in Fig. 9. Along the [100] direction the four Co^{2+} sites in the unit cell all make the same angle with the applied magnetic field **B**. We therefore see only a single ODMR transition as in Fig. 9(a). When the applied magnetic field is along the [111] direction, the four ⟨111⟩-type centers are no longer equivalent; the center aligned along the magnetic field is distinguished from the other three. In this case we expect to see two ODMR transitions as observed in Fig. 9(b). The low-field ODMR transition shows a reduction in the MCD signal as expected. On the other hand, the high-field ODMR transition appears to show an *increase* in the total MCD signal. The total MCD signal observed is a combination of the parallel MCD signal and the MCD signals from the other three centers. The MCD signal for the parallel center must therefore be opposite in sign to that from the other centers. For the example shown in Fig. 3, this would mean that the Zeeman splitting of the ground or excited states for the parallel center is opposite to that for the other three centers. We find that, as the magnetic field is rotated away from the [111] direction, the intensity of the "positive" ODMR lines weakens (Fig. 10) and eventually the ODMR lines become negative. This result is a further demonstration that the site occupied by the Co^{2+} ion has an axis of symmetry along ⟨111⟩-type directions. Along the [111] direction the coupling between the Kramers doublets participating in the MCD signal with all the other Kramers doublets within the d^7 shell is at a minimum. Rotating the magnetic field **B** away from [111] results in an admixture into the ground and excited states which eventually leads to a reversal of the Zeeman splitting as the magnetic field approaches the [100] and [011] directions (Fig. 10). This effect was also observed by Ahlers *et al.*[22] for the $Tl^0(1)$ center in KCl. While this give a qualitative explanation for the observed effect, the microscopic origin for this reversal of the Zeeman splitting has not been determined.

The ODMR line positions in Fig. 10 can be fitted to the spin Hamiltonian in Eq. (15) with the two independent g values, $g_{\parallel}=2.215$, $g_{\perp}=4.628$. The fit to the experimental data is shown as the solid lines in Fig. 10. These g values indicate that the observed ODMR transitions are within the $\pm\frac{1}{2}$ levels of the ground state and so the sign of the fine-structure parameter D is positive from Eq. (14). As $g_{\perp}/2>g_{\parallel}$, we are again led to the conclusion from Eq. (16) that the orbital doublets arising from the orbital triplet manifolds are lower in energy than the orbital singlets. At the low temperatures of the MCD-ODMR experiments the population of the $\pm\frac{3}{2}$ levels is very small and so no signals were observed in this doublet. From Eq. (17) we estimate the spin-orbit constant to be $\lambda=-193$ cm^{-1}. We can also estimate λ from Eq. (14). In doing this we use the theoretical estimate for the positions of the $^4T_2$ doublet and singlet split levels and in this case we find $\lambda=-190$ cm^{-1}. Both values are quite similar but somewhat surprising as we would normally expect to see a reduction in λ from the free-ion case.

Both the ODMR and the optical zero-phonon linewidths are quite broad. The ODMR linewidth is 20 mT and exhibits no resolved hyperfine structure associated with the ^{57}Co nucleus (100% abundant) which has a nuclear spin of $I=\frac{7}{2}$. We noted earlier that the inhomogeneous optical zero-phonon transition linewidth is 24 cm^{-1} so that the large ground-state splitting could not be resolved. The Co^{2+} ion substitutes for Ga^{3+} in the lattice and some charge compensation is thus required to maintain charge neutrality. Both of these broad linewidths are probably due to a distribution of positions for the charge compensating ions which would result in a distribution of strains at the sites of the substitutional Co^{2+} ions in the $LiGa_5O_8$ lattice. At present we do not know what species is providing the charge compensation for the Co^{2+}. It is interesting to note that the behavior shown in Fig. 10 is consistent with the C_3 symmetry deduced from the crystal structure, and this would imply that either the charge compensating ion is far away from the Co^{2+} ion or located along a ⟨111⟩-type direction.

VI. CONCLUSIONS

The optical spectra of Co^{2+} in $LiGa_5O_8$ provide clear evidence that the Co^{2+} ions substitute for tetrahedrally coordinated Ga^{3+} ions in this lattice and therefore occupy sites of C_3 symmetry, as illustrated in Fig. 2. We have presented a detailed crystal-field model for the Co^{2+} ion in this site, and we have deduced the crystal-field parameters. Strong luminescence with a lifetime of 200 ns is observed to three lower levels from the $^4T_1(^4P)$ level. In a previous publication this system was suggested as a possible candidate as a visible-infrared laser system.[9] Further experiments to look at excited-state absorption effects would have to be undertaken to determine the potential of $LiGa_5O_8$:Co^{2+} as a laser system. Within the accuracy of the ODMR experiment, the site symmetry of the Co^{2+} ion is C_3, suggesting that charge compensating ions are either far removed from the Co^{2+} or are along the C_3 axis.

ACKNOWLEDGMENTS

We would like to express our gratitude to Professor G. D. Watkins of Lehigh University where the MCD-

ODMR measurements were performed. This work was supported in part by Optronics Ireland, a division of EOLAS, and by the Air Force Office of Scientific Research, Air Force Systems Command, USAF, under Grant No. AFOSR 88-0355. The work carried out at Lehigh University (by FGA and JFD) was supported by the U.S. Office of Naval Research, under Grant No. N00014-90-J-1264 and by the National Science Foundation under Grant No. DMR-85-20269. The Ge detector was obtained through a grant from the University College Galaway Development Fund which we gratefully acknowledge.

---

[1] R. Pappalardo, D. L. Wood, and R. C. Linares, Jr., J. Chem. Phys. **35**, 2041 (1961).

[2] D. L. Wood and J. P. Remeika, J. Chem. Phys. **46**, 3595 (1967).

[3] T. J. Glynn, L. Kelleher, G. F. Imbusch, D. M. Larkin, F. R. Merritt, and M. J. Berggren, J. Chem. Phys. **55**, 2925 (1971).

[4] E. W. Gorter, Philips Res. Rep. **9**, 295 (1954).

[5] T. J. Glynn, J. P. Larkin, G. F. Imbusch, D. L. Wood, and J. P. Remeika, Phys. Lett. **30A**, 189 (1969).

[6] T. Abritta, N. V. Vugman, F. de Souza Barros, and N. T. Melamed, J. Lumin. **31&32**, 281 (1984).

[7] C. McShera, P. J. Colleran, T. J. Glynn, G. F. Imbusch, and J. P. Remeika, J. Lumin. **28**, 41 (1983).

[8] J. F. Donegan, F. J. Bergin, T. J. Glynn, G. F. Imbusch, and J. P. Remeika, J. Lumin. **35**, 57 (1986).

[9] J. F. Donegan, G. P. Morgan, T. J. Glynn, and G. Walker, J. Mod. Opt. **37**, 769 (1990).

[10] R. M. Macfarlane and J.-C. Vial, Phys. Rev. B **34**, 1 (1986).

[11] J. Ferguson, D. L. Wood, and L. G. Van Uitert, J. Chem. Phys. **51**, 2904 (1969).

[12] C. E. Moore, *Atomic Energy Levels,* Natl. Bur. Stand. (U.S.) Circ. No. 467 (U.S. GPO, Washington, D.C., 1952), Vol. II, p. 85.

[13] R. M. Macfarlane, J. Chem. Phys. **39**, 3118 (1963).

[14] The authors would like to thank Professor F. S. Ham for helpful discussions on this point.

[15] J. S. Griffith, *The Theory of Transition-Metal Ions* (Cambridge University, Cambridge, 1961), p. 437.

[16] G. E. Pake and T. L. Estle, *The Physical Principles of Electron Paramagnetic Resonance* (Benjamin, London, 1973), p. 127.

[17] B. Henderson and G. F. Imbusch, *Optical Spectroscopy of Inorganic Solids* (Oxford Science, Oxford, 1989), p. 130.

[18] M. D. Sturge, M. J. Guggenheim, and M. H. L. Pryce, Phys. Rev. B **2**, 2459 (1970).

[19] A. Lempicki, L. Andrews, S. J. Nettel, and B. C. McCollum, Phys. Rev. Lett. **44**, 1234 (1980).

[20] J. F. Donegan, T. J. Glynn, and G. F. Imbusch, J. Lumin. **45**, 23 (1990).

[21] R. M. Macfarlane and J.-C. Vial, Mater. Sci. Forum **10-12**, 845 (1986).

[22] F. J. Ahlers, F. Lohse, J.-M. Spaeth, and L. K. Mollenauer, Phys. Rev. B **28**, 1249 (1983).